Available online at www.sciencedirect.com
SCIENCE DIRECT
Acta Materialia 54 (2006) 2015–2026
Acta MATERIALIA
www.actamat-journals.com

Phase-field simulation of the columnar-to-equiaxed transition in alloy solidification

Arnoldo Badillo, Christoph Beckermann *

Department of Mechanical and Industrial Engineering, 2412 Seamans Center, University of Iowa, Iowa City, IA 52242 1527, USA

Received 22 November 2005; accepted 20 December 2005
Available online 23 February 2006

Abstract

The columnar-to-equiaxed transition (CET) in directional solidification of alloys is simulated using the phase-field method. The method relies on the solution of a solute conservation equation and an equation for the propagation of the phase field on the scale of the developing microstructure. A parametric study is performed to investigate the effects of the applied temperature gradient and pulling speed, the seed spacing and nucleation undercooling for the equiaxed grains, and the crystalline anisotropy strength on the CET. The results qualitatively agree with a previously developed analytical model of the CET. At relatively high pulling speeds, a mixed columnar–equiaxed structure is found to be stable over a range of temperature gradients. Furthermore, the CET depends sensitively on the anisotropy strength. The simulations also reveal the presence of primary spacing adjustments during purely columnar growth due to nucleation of seeds, and deactivation of seeds by solutal interactions from nearby growing grains.

Keywords: Directional solidification; Metal alloys; Columnar/equiaxed microstructure; Phase-field models

1. Introduction

The columnar-to-equiaxed transition (CET) in the grain structure of metal alloy castings has fascinated researchers in the solidification area for more than 50 years [1]. The CET is usually assumed to occur when the advance of the columnar front is blocked by equiaxed grains that grow in the constitutionally undercooled liquid ahead of the columnar dendrites. Based on this idea, Hunt [2] developed an analytical model that predicts the CET during directional solidification as a function of the applied temperature gradient, the solidification speed, and the nucleation undercooling and number density of equiaxed grains. This model has been extended and improved by several researchers [3–5]. A simulation model that relies on the solution of averaged conservation equations that are coupled to nucleation and growth laws has been presented by Beckermann and co-workers [6,7]. More complex models have followed the nucleation and growth of each individual grain (e.g., Refs. [8–12]). By predicting the size, orientation, and shape of each grain, the location of the CET in a casting can be inferred directly from the appearance of the calculated grain structure. These studies rely on the same type of dendrite tip growth models for the evolution of the grain envelopes as the previous modeling studies [2–7]. A solute diffusion equation is not solved, and the motion of the solid–liquid interface on a microscopic scale is not resolved.

With recent advances in computational power, direct microstructure simulation techniques hold some promise for modeling the CET. Spittle and Brown [13], Nastac [14], and Dong and Lee [15] have applied so-called coupled cellular automaton finite difference (CA-FD) methods to simulate the CET in metal alloy castings. In this class of methods, the solid–liquid interface is tracked directly on the numerical grid and its motion is determined from the numerical solution of a solute diffusion equation on a microscopic scale. Grain envelopes are

* Corresponding author. Tel.: +1 319 335 5681; fax: +1 319 335 5669.
E-mail address: becker@engineering.uiowa.edu (C. Beckermann).

1359-6454/$30.00
doi:10.1016/j.actamat.2005.12.025

not considered and no use is made of separate dendrite tip growth models. While the CA-FD methods produce realistic-looking dendritic growth patterns and have resulted in much insight into the CET, some questions remain regarding their accuracy. Independence of the results on the numerical grid size is rarely demonstrated. Furthermore, the CA-FD techniques often rely on relatively arbitrary rules for incorporating the effects of crystallographic orientation while propagating the solid–liquid interface. For example, in the most recent and advanced study using a CA-FD technique [15], the strength of the surface energy anisotropy is not even specified. It is now well accepted that dendritic growth of crystalline materials depends very sensitively on the surface energy anisotropy [16,17].

The phase-field method has also become a popular technique for the direct numerical simulation of microstructure evolution in solidification [18]. However, progress in modeling solidification of alloys using the phase-field method has been relatively slow. The first fully quantitative phase-field model that allows for unequal solute diffusivities in the liquid and solid was only developed in 2001 [19]. This model has been extended by Ramirez et al. [20] to account for coupled heat and solute diffusion and by Echebarria et al. [21] to directional alloy solidification with an applied temperature gradient. Recently, Ramirez and Beckermann [22] used this phase-field model to study free dendritic growth of alloy dendrites. These studies clearly demonstrate that the phase-field method allows for accurate and fully grid-independent simulations of alloy solidification on the scale of the microstructure.

The objective of the present study is to perform direct numerical simulations, in two spatial dimensions, of the CET in alloy solidification using the phase-field model of Refs. [20,21]. The phase-field model equations are briefly summarized in the next section. The numerical procedures are explained in Section 3. Section 4 presents the results of numerous simulations where the CET is studied as a function of the applied temperature gradient and pulling speed, the equiaxed grain nucleation undercooling and number density, and the crystalline anisotropy. In addition, the results are compared to the original CET model of Hunt [2]. The conclusions of the study are summarized in Section 5.

2. Phase-field model

The phase-field model employed here allows for the simulation of microstructural patterns during the solidification of dilute binary alloys. It has been derived and extensively validated by Ramirez et al. [20] and Echebarria et al. [21]. The model neglects the solute diffusivity in the solid, and all material properties are assumed constant. It reduces to the sharp interface equations in a thin interface limit where the width of the diffuse interface is smaller than the radius of curvature of the interface but larger than the real width of a solid–liquid interface, and when kinetic effects are negligible. The anti-trapping current concept of Karma [19] is applied to recover local equilibrium at the interface and eliminate interface stretching and surface diffusion effects that arise when the solute diffusivities are unequal in the solid and liquid.

Let ϕ represent the phase field, where $\phi = 1$ in the bulk solid phase and $\phi = -1$ in the bulk liquid phase. The phase field varies smoothly between these bulk values within the diffuse interface region. The anisotropic and dimensionless forms of the phase-field and species equations, for a vanishing kinetic effect, are given in two-dimensional form, respectively, by [20,21]

$$\begin{aligned}[1+(1-k)U]a_s(\hat{n})^2\frac{\partial\phi}{\partial t} &= \vec{\nabla}\cdot(a_s(\hat{n})^2\vec{\nabla}\phi) \\ &+ \partial_x\left(\left|\vec{\nabla}\phi\right|^2 a_s(\hat{n})\frac{\partial a_s(\hat{n})}{\partial(\partial_x\phi)}\right) \\ &+ \partial_y\left(\left|\vec{\nabla}\phi\right|^2 a_s(\hat{n})\frac{\partial a_s(\hat{n})}{\partial(\partial_y\phi)}\right) \\ &+ \phi-\phi^3-\lambda(1-\phi)^2(U+\theta),\end{aligned} \tag{1}$$

$$\left(\frac{1+k}{2}\right)\frac{\partial U}{\partial t} = \vec{\nabla}\cdot\left(\tilde{D}\frac{1-\phi}{2}\vec{\nabla}U+\vec{j}_{at}\right) + \frac{1}{2}\frac{\partial}{\partial t}\{\phi[1+(1-k)U]\}, \tag{2}$$

where $\hat{n} = -\vec{\nabla}\phi/\left|\vec{\nabla}\phi\right|$ is the unit vector normal to the interface, $a_s(\hat{n}) = 1+\varepsilon\cos(4\phi)$ is a function that describes the surface energy anisotropy, $\phi = \arctan(\partial_y\phi/\partial_x\phi)$ is the angle between the direction normal to the interface and the horizontal axis, ε is a dimensionless parameter that characterizes the anisotropy strength, k is the partition coefficient, x and y are the spatial coordinates, and t is time. In the present study, the crystal axes are always aligned with the coordinate axes. The anti-trapping current $\vec{j}_{at}$ is given by [19]

$$\vec{j}_{at} = \frac{1}{2\sqrt{2}}[1+(1-k)U]\frac{\partial\phi}{\partial t}\frac{\vec{\nabla}\phi}{\left|\vec{\nabla}\phi\right|} \tag{3}$$

which is non-zero only inside the diffuse interface region.

The time and length scales used to non-dimensionalize equations (1) and (2) are $\tau_0 = (d_0^2/D)a_2\lambda^3/a_1^2$ and $W_0 = d_0\lambda/a_1$, which represent a relaxation time and a measure of the interface width, respectively. Here, d_0 is the chemical capillary length and D is the solute diffusivity in the liquid phase. The dimensionless solute diffusivity is given by $\tilde{D} = D\tau_0/W_0^2$ and λ is a dimensionless coupling parameter, which is chosen as $\lambda = \tilde{D}/a_2$ to simulate kinetics-free growth ($a_1 = 0.8839$, $a_2 = 0.6267$) [23]. The coupling constant λ is the only free parameter and the results should be independent of λ when they are converged. Decreasing λ corresponds to decreasing the diffuse interface width, since $\lambda = a_1 W_0/d_0$.

The dimensionless solute concentration is given by

$$U = \frac{\left(\frac{2Ck/C_\infty}{1+k-(1-k)\phi}\right) - 1}{1-k}, \tag{4}$$

where C is a "mixture" concentration (in wt.%) that varies smoothly within the diffuse interface, between the values of the concentration in the bulk liquid and solid phases, and C_∞ is the initial alloy concentration far from the solidification front.

In the present simulations of directional solidification, the temperature is imposed and given by a linear profile that translates across the domain in the x-direction. In dimensional terms, the temperature distribution $T(x,t)$ is given by

$$T = T_0 + G(x - V_p t), \tag{5}$$

where T_0 is a reference temperature, G is the imposed thermal gradient, and V_p is the imposed ("pulling") speed with which the profile is translated across the domain. The dimensionless temperature θ in Eq. (1) is defined as

$$\theta = \frac{T - T_s(C_\infty)}{\Delta T_0}, \tag{6}$$

where $\Delta T_0 = T_l(C_\infty) - T_s(C_\infty) = |m|C_\infty(1-k)/k$ is the equilibrium freezing temperature range corresponding to C_∞, $T_l(C_\infty)$ and $T_s(C_\infty)$ are the liquidus and solidus temperatures, respectively, corresponding to C_∞, and m is the slope of the liquidus line in the equilibrium phase diagram. Note that the freezing range also relates the chemical capillary length to the commonly used Gibbs–Thomson coefficient Γ through $\Gamma = d_0\Delta T_0$.

3. Computational procedures and validation

The governing equations were solved numerically using the same discretization scheme as in Ramirez et al. [20]. Unless otherwise noted, the grid spacing used in the finite difference scheme was equal to $\Delta x/W_0 = 0.8$. A schematic of the computational domain used in the present directional solidification simulations is shown in Fig. 1. The simulations were initialized with a thin solid layer along the left domain wall (at $x = 0$). The solid–liquid interface was initialized as planar except for a small perturbation with an amplitude that satisfies $\delta \gg W_0$. The reference temperature T_0 in Eq. (5), which is nothing but the initial temperature of the left domain wall, was chosen to be equal to or slightly below $T_s(C_\infty)$. The initial value for the dimensionless concentration U was taken as -1 ($C = C_\infty$), except in the validation study presented next. The length of the computational domain in the x-direction was chosen long enough that the temperature at the right domain wall is always greater than $T_l(C_\infty)$, and that the solute concentration is undisturbed by solidification and uniformly equal to C_∞. Zero-flux boundary conditions for the phase-field and solute conservation equations were applied at all domain walls. Full advantage was taken of symmetry in the solidification pattern when choosing the height of the computational domain in the y-direction.

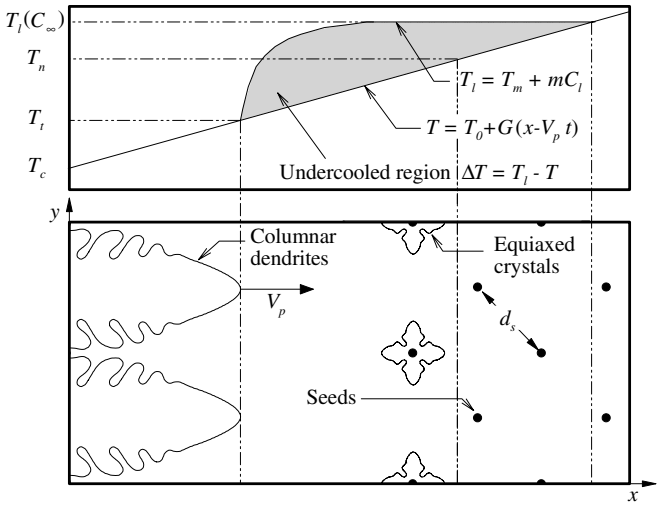

Fig. 1. Schematic of the computational domain used in the numerical simulations of the CET in directional solidification; the temperature gradient G is translated in the x-direction with a constant speed V_p.

The model and the numerical implementation were validated extensively through comparisons with analytical solutions and other available benchmark results. The reader is referred to Ref. [20] for details of these studies. Here, only the results of one validation study are presented. The validation study is adopted from Echebarria et al. [21] and involves the well-known Mullins–Sekerka instability [24] in the directional solidification of a dilute binary alloy. Fig. 2 shows a schematic of the physical system considered. A sinusoidal perturbation of wavelength λ_f (or wave number $Q = 2\pi/\lambda_f$) is applied to a planar solidification front. The concentration field U is initialized according to the analytical solution for steady state, directional alloy solidification with a planar front [25]; accordingly, the initial solute concentration in the liquid decays exponentially away from the interface. The properties used in the simulations

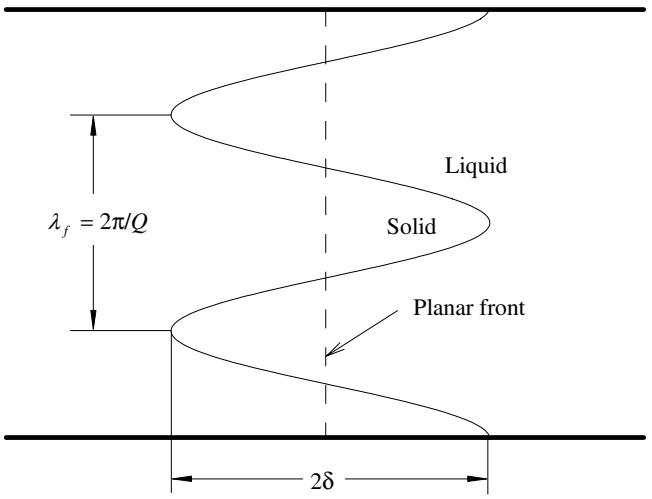

Fig. 2. Schematic of the sinusoidal perturbation applied to a planar front in the Mullins–Sekerka instability test case.

correspond to impure succinonitrile and are summarized in Table 1. The simulation parameters are also provided in Table 1; the thermal and solutal diffusion lengths are defined, respectively, as $l_T = \Delta T_0/G$ and $l_D = 2D/V_p$. For a given wave number, the computed phase-field contours are used to measure the amplitude 2δ of the growing perturbation as a function of time. The amplitude growth rate $\dot{\delta}$ is then determined by fitting the amplitudes to an exponential curve, as explained in Ref. [21]. The dimensionless growth rate is defined as $\chi = (\dot{\delta}\tau_0/W_0)/(\delta/W_0)$. Fig. 3(a) shows how the amplitude growth rate varies with the dimensionless interface width, $W_0/d_0 = \lambda/a_1$, in the phase-field model. These calculations are for a relatively large dimensionless wave number of $Ql_D = 87.3$. It can be seen that the growth rate approaches the theoretical value from the Mullins–Sekerka analysis [24] as the interface width is decreased. The phase-field model results can be considered converged for W_0/d_0 less than about 10. A comparison of computed growth rates with the analytically obtained Mullins–Sekerka stability spectrum is shown in Fig. 3(b). Overall, the growth rates obtained from the phase-field simulations agree well with the theoretical values, despite the use of a relatively large interface width of $W_0/d_0 = 18.05$. The agreement improves with decreasing wave number. Additional results in Ref. [21] indicate that a smaller grid spacing $\Delta x/W_0$ than the one used here (0.8) produces only slightly more accurate results.

In the simulations of the CET presented in the next section, an interface width of $W_0/d_0 = 11.3$, corresponding to $\lambda = 10$, is utilized. Based on Fig. 3 and additional numerical tests not presented here, this value for λ is small enough to provide results that are reasonably independent of the interface width. Using an interface width that is even smaller is difficult due to escalating computational times [20,21]. Other details of the CET simulations are described next. First, a columnar structure is allowed to evolve from the perturbed planar solidification front with which the simulations are initialized (see above). The simulations are continued until the columnar structure reaches a steady growth regime where the temperature of the tips T_t (see Fig. 1) reaches a constant value. At that time, small seeds for the nucleation of equiaxed grains are introduced into the computational domain at certain locations ahead of the columnar front, as illustrated in Fig. 1. The seeds can be thought

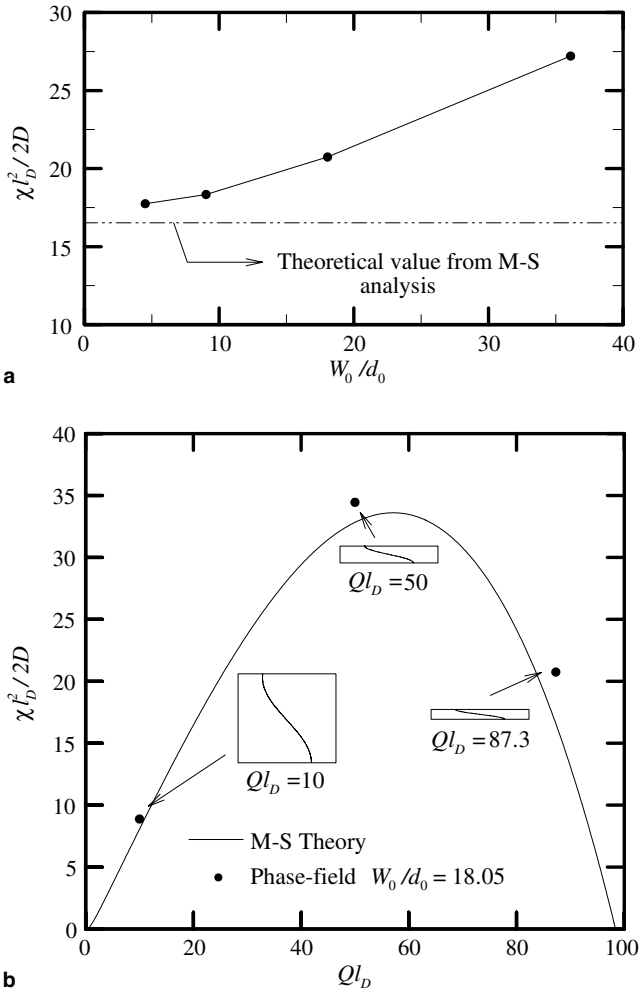

Fig. 3. Comparison of the dimensionless growth rate χ of the perturbation amplitude between the phase-field simulations and the Mullins–Sekerka analysis [24]: (a) convergence of the growth rate with respect to the diffuse interface width W_0/d_0 for a dimensionless wave number of $Ql_D = 87.3$; (b) results for the entire stability spectrum using $W_0/d_0 = 18.05$.

Table 1
Parameters and properties for the impure succinonitrile alloy simulations [21]

$\|m\|C_\infty$, shift in the melting point (K)	2
D, diffusion coefficient ($\mu m^2/s$)	1000
Γ, Gibbs–Thomson coefficient (K μm)	6.48×10^{-2}
V_p, pulling speed (μm/s)	32
G, thermal gradient (K/cm)	140
d_0, chemical capillary length (μm)	1.3×10^{-2}
l_T, thermal length (μm)	333
l_D, diffusion length (μm)	62.5
ε, anisotropy	0.007
k, partition coefficient	0.3

of as grain refiner particles of a certain size. The term nucleation is used here loosely and simply denotes the initiation of the growth of a grain; in the presence of inoculant particles, the onset of free growth is actually not nucleation controlled [26,27]. The seeds are characterized by a regular spacing d_s (see Fig. 1) and a certain nucleation undercooling $\Delta T_n = T_l(C_\infty) - T_n$. In two dimensions, the spacing is related to the seed number density by $n_s = d_s^{-2}$. If the local constitutional undercooling in the melt $\Delta T = T_l(C) - T$ at the location of a seed reaches ΔT_n, an equiaxed crystal is allowed to grow there. Note that the local constitutional undercooling in the melt ΔT is measured relative to the liquidus temperature corresponding to the local solute concentration, i.e., $T_l(C)$, not $T_l(C_\infty)$. The simulations are then continued until the new grain structure reaches a steady growth regime.

In order to avoid the need for a very long computational domain for large simulation times, the following moving-domain technique was implemented. When the temperature

of the left domain wall (at $x = 0$) reaches a certain cut-off temperature T_c (see Fig. 1), all fields are shifted by one grid point to the right. In other words, one line of grid points is removed at the left side, and one line of grid points is added on the right side. This shifting of grid points takes place at time intervals equal to $\Delta x/V_p$. The values for ϕ and U on the grid points that are removed on the left side (and, hence, correspond to the temperature T_c) are stored in a computer file for later plotting. The new grid points that are added on the right side are assigned values of $\phi = -1$ (liquid) and $U = -1$ ($C = C_\infty$). The value of the cut-off temperature T_c is chosen to correspond to a location well behind the columnar tips where the melt is no longer undercooled. Comparisons were performed of simulations with and without the moving-domain technique to verify that the value chosen for T_c is sufficiently low to eliminate any dependency of the predicted solidification pattern on T_c. The values chosen for T_c are provided in the next section together with the results of each simulation. With the moving-domain technique, and fully exploiting symmetry in the y-direction, the number of grid points used in a simulation of the CET was typically equal to 2000×151.

4. Results and discussion

The CET simulations presented in the following correspond to an Al–3 wt.% Cu alloy whose properties are summarized in Table 2. A total of 29 simulations were performed where the temperature gradient G, the pulling speed V_p, the equiaxed seed spacing d_s, the nucleation undercooling ΔT_n, and the crystalline anisotropy strength ε were varied. The conditions for each simulation case are provided in Table 3.

4.1. Steady columnar growth

Before discussing the CET, it is useful to examine in detail the predictions for steady columnar growth. Recall that in all simulations, the columnar structure is allowed to reach a steady growth stage before (equiaxed grain) seeds are introduced into the computational domain.

Fig. 4 shows an example of computed phase field and solute concentration fields when the columnar structure has reached a steady growth stage. The simulation corresponds to Case 4 in Table 3. The columnar dendrite can be seen to have grown several secondary branches behind the primary tip. A thin solute concentration boundary layer exists in the liquid along the primary tip contour. In this boundary layer, the concentration decreases exponentially to C_∞ ($U = -1$). The concentrations in the solid indicate the presence of a complex microsegregation pattern. The solute concentrations in the liquid, as shown in Fig. 4(a), can be converted into a constitutional undercooling, defined as

Table 2
Parameters and properties for the Al–3 wt.% Cu alloy simulations

m, liquidus slope [25] (K/wt.%)	−2.6
C_∞, alloy composition (wt.%)	3
D, liquid diffusion coefficient [25] (μm^2/s)	3000
Γ, Gibbs–Thomson coefficient [25] (K μm)	0.24
d_0, chemical capillary length (μm)	5×10^{-3}
ε, anisotropy [28]	0.01
k, partition coefficient [25]	0.14

Table 3
Conditions for the simulations of the CET, and final grain structure obtained

Case	G (K/cm)	V_p (μm/s)	ε (%)	d_s (μm)	ΔT_n (K)	Structure
1	140	3000	1	9.7	8	Equiaxed
2	140 × 10	3000	1	9.7	8	Equiaxed
3	140 × 20	3000	1	9.7	8	Equiaxed
4	140 × 40	3000	1	9.7	8	Equiaxed
5	140 × 50	3000	1	9.7	8	Equiaxed
6	140 × 60	3000	1	9.7	8	Columnar
7	140 × 70	3000	1	9.7	8	Columnar
8	140 × 150	3000	1	9.7	8	Columnar
9	140 × 50	6000	1	9.7	8	Equiaxed
10	140 × 70	6000	1	9.7	8	Equiaxed
11	140 × 150	6000	1	9.7	8	Mixed
12	140 × 280	6000	1	9.7	8	Columnar
13	140 × 50	10,000	1	9.7	8	Equiaxed
14	140 × 110	10,000	1	9.7	8	Mixed
15	140 × 150	10,000	1	9.7	8	Mixed
16	140 × 280	10,000	1	9.7	8	Mixed
17	140 × 400	10,000	1	9.7	8	Mixed
18	140	1000	1	9.7	8	Columnar
19	140	1500	1	9.7	8	Equiaxed
20	140 × 50	1500	1	9.7	8	Columnar
21	140 × 50	2500	1	9.7	8	Columnar
22	140 × 50	3500	1	9.7	8	Equiaxed
23	140 × 50	4500	1	9.7	8	Equiaxed
24	140 × 40	3000	1	19.4	8	Equiaxed
25	140 × 40	3000	1	38.8	8	Columnar
26	140 × 60	3000	1	9.7	7	Equiaxed
27	140 × 40	3000	0.5	9.7	8	Equiaxed
28	140 × 40	3000	1.2	9.7	8	Columnar
29	140 × 40	3000	3	9.7	8	Columnar

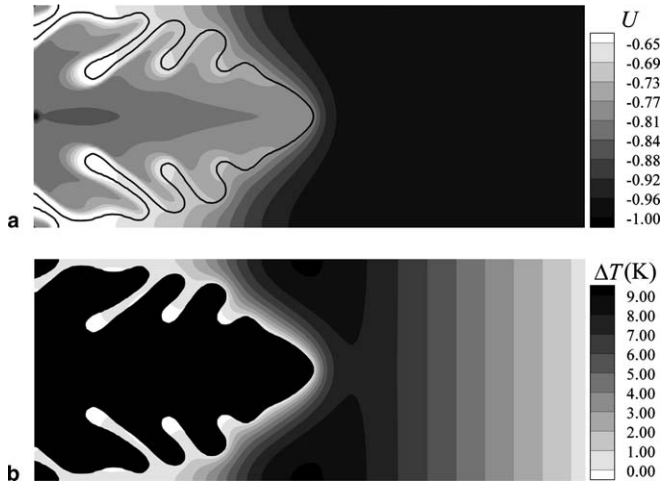

Fig. 4. Close-up of calculated dimensionless concentration (a) and constitutional undercooling (b) fields for Case 4 during steady columnar growth, before the nucleation of equiaxed grains.

$\Delta T = T_l(C) - T$, where $T_l(C)$ is the equilibrium liquidus temperature corresponding to the computed local solute concentration in the melt, C, and T is the local temperature. The result is shown in Fig. 4(b). Far ahead of the dendrite, the undercooling varies in a linear fashion in accordance with the imposed temperature field, since the solute concentration is uniformly at C_∞, and T_l is therefore constant. At the right domain boundary, the undercooling has almost vanished. The undercooling is also close to zero at the solid–liquid interface, since it is in equilibrium (other than for the local curvature undercooling, which is not taken into account when calculating T_l). Relatively small undercoolings exist as well in the melt between the secondary dendrite branches behind the primary tip. The largest undercoolings are present just ahead of the solute concentration boundary layer along the primary tip contour. It is in these regions of large undercooling where the equiaxed grains will nucleate first. Interestingly, the maximum undercooling is not observed directly ahead of the primary tip on the central columnar dendrite axis, but on the symmetry line between columnar branches (i.e., at the upper and lower domain boundaries). This was also noted by Dong and Lee [15].

The variations of the solute concentrations and the solid fraction during steady columnar growth are further investigated in Fig. 5. The results in this figure correspond to Case 7 in Table 3. Fig. 5(a) shows that in this case the steady columnar solidification pattern consists of cells of a certain spacing. The variation of the computed solute concentration along a vertical line ($x = 54$ μm) near the cell tips (Cut A in Fig. 5(a)) is plotted in Fig. 5(c). The concentration in the liquid decays exponentially away from the solid–liquid interface, with a minimum at the symmetry line between the cells. In the solid, the concentrations are much lower (since the partition coefficient is equal to 0.14) and relatively uniform. The values for the average concentrations in the liquid $\overline{C}_l$ and solid $\overline{C}_s$ are also indi-

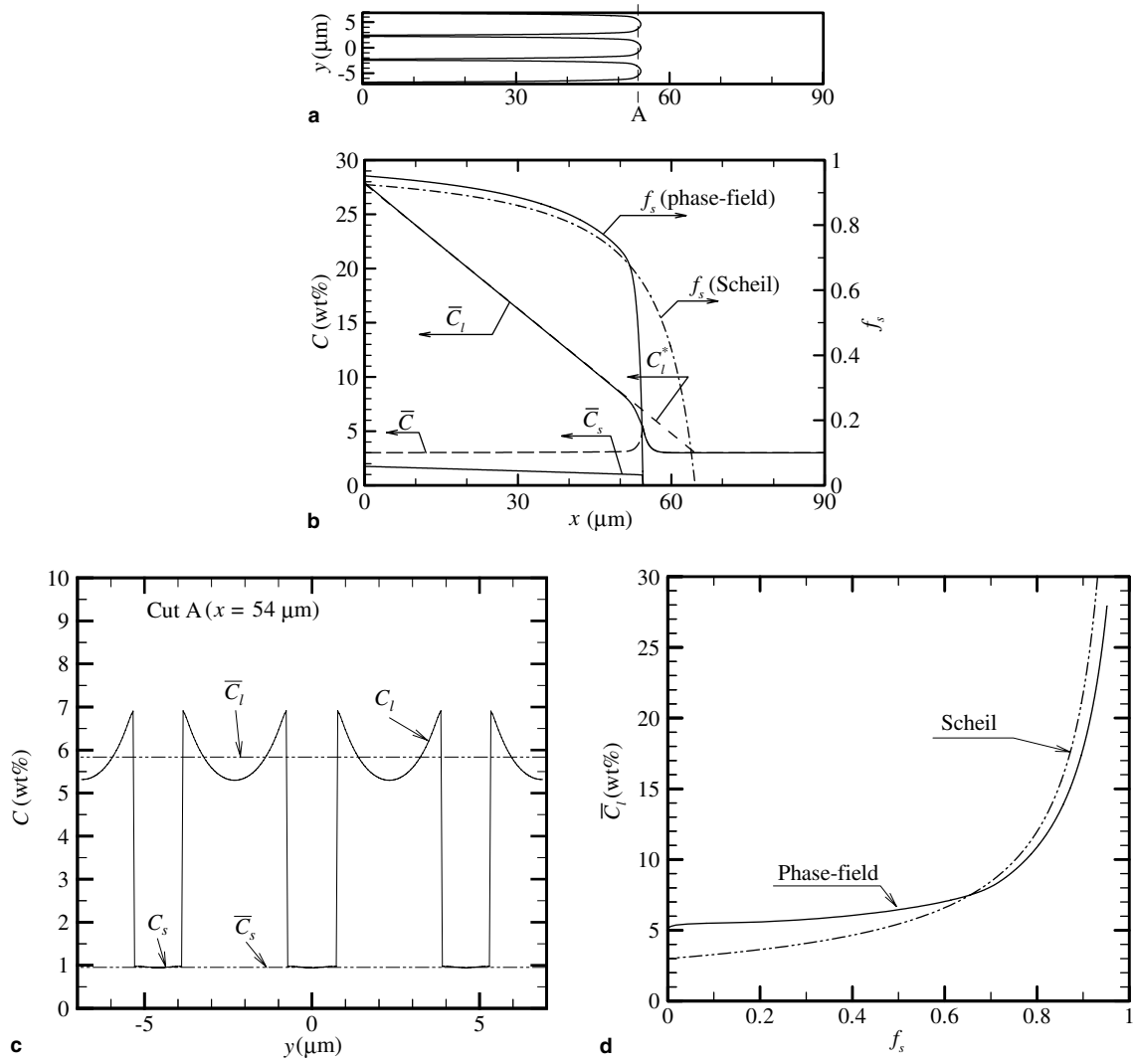

Fig. 5. Solute concentration and solid fraction variations during steady columnar growth for Case 7: (a) calculated solidification pattern; (b) variation of solute concentrations, averaged along the y-direction, and the solid fraction in the direction of the applied temperature gradient; (c) variation of the solute concentration along the y-direction at $x = 54$ μm (Cut A); and (d) variation of the averaged liquid concentration with solid fraction and comparison with the Scheil equation.

cated in Fig. 5(c). These values were obtained by averaging the calculated concentrations separately in the liquid and solid along the vertical line corresponding to Cut A. By performing this averaging for all grid lines along the direction of the imposed temperature gradient, a smooth variation of the average liquid and solid concentrations with x can be obtained, as shown in Fig. 5(b). The same averaging procedure was applied to the phase field ϕ, and the resulting variation of the solid fraction f_s with x is also plotted in Fig. 5(b). Additionally, Fig. 5(b) includes the variation of the average mixture concentration, defined as $\overline{C} = (1 - f_s)\overline{C}_l + f_s\overline{C}_s$. It can be seen that the solid fraction increases steeply with distance behind the cell tips; once the solid fraction reaches about 0.7, the f_s variation is much more gradual, as expected from the deep liquid grooves in Fig. 5(a). The average liquid concentration decreases with increasing x in accordance with the linear variation of the liquidus concentration $C_l^*(T)$, except near the cell tips. There, $\overline{C}_l$ decreases more steeply in accordance with the liquid concentration fields already discussed in connection with Fig. 4(a), and $\overline{C}_l$ reaches C_∞ about 5 μm ahead of the cell tips. The area between the $C_l^*(T)$ and $\overline{C}_l$ lines in Fig. 5(b) indicates the region where the melt is, on the average, constitutionally undercooled, i.e., $\overline{C}_l < C_l^*(T)$; this region extends from about 2.3 μm behind the tips to about 10 μm in front of the tips. Note that the average mixture concentration $\overline{C}$ is not everywhere equal to C_∞ (=3 wt.%). This can be explained by the fact that $\overline{C}$ must be equal to $\overline{C}_l$ ahead of the tips ($f_s = 0$), where $\overline{C}_l$ shows the steep decrease mentioned above. Since the $\overline{C}$ variation with x must be continuous, $\overline{C}$ must increase already behind the tips. Solute is nonetheless conserved in the simulations: the additional solute present near the tips (i.e., where $\overline{C} > C_\infty$) originates from an initial transient not shown in Fig. 5. Finally, the calculated variation of the average liquid concentration with solid fraction from the phase-field simulation is compared with the Scheil equation, $\overline{C}_l = C_l^*(T) = C_\infty(1 - f_s)^{k-1}$, in Fig. 5(d). As expected, the general trend in the two $\overline{C}_l(f_s)$ curves is the same. Due to the solute gradients in the liquid near the tips, the phase-field results show higher average liquid concentrations for small solid fractions. Note that in the Al–Cu system, the eutectic does not form until the solute concentration in the liquid reaches about 33.1 wt.%.

The variation of the constitutional undercooling in the liquid during steady columnar growth is further explored in Fig. 6. Here, the undercooling is plotted along a newly defined z-coordinate, which is in the same direction as the x-coordinate but has its origin at the x-position of the columnar tips, as shown in the insets. Fig. 6(a) shows the variation of the undercooling along the central columnar dendrite axis, and Fig. 6(b) that along the symmetry line between two columnar branches. Results are included for six different imposed thermal gradients G, corresponding to Cases 1 and 3–7 in Table 3. It can be seen from Fig. 6(a) that the maximum undercooling in the liquid along the central dendrite axis depends only weakly on

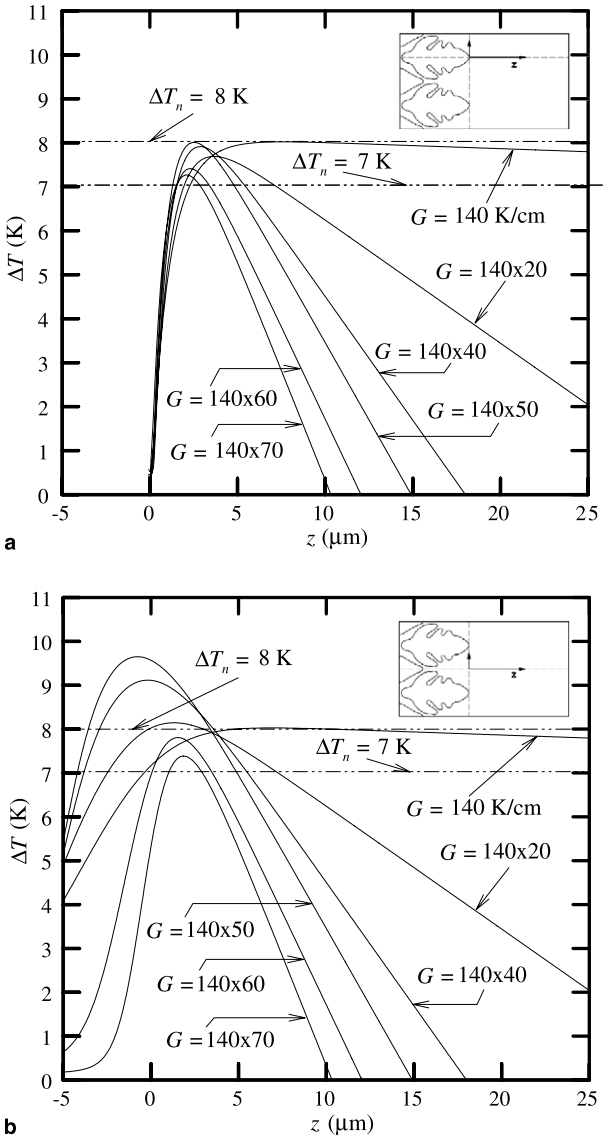

Fig. 6. Variation of the constitutional undercooling during steady columnar growth in front of the dendrite tips (a) and along the centerline between the columnar branches (b) for different applied temperature gradients ($V_p = 3000$ μm/s, $d_s = 9.7$ μm, and $\varepsilon = 0.01$).

the thermal gradient and varies between about 7 and 8 K for the cases considered here. If the nucleation undercooling ΔT_n were greater than 8 K, no equiaxed grains could form directly ahead of the primary tips; for $\Delta T_n = 7$ K, on the other hand, nucleation would take place regardless of the thermal gradient. As shown in Fig. 6(b), the maximum undercooling along the symmetry line between columnar branches is generally larger than in Fig. 6(a) and varies between about 7 and 10 K depending on the thermal gradient; also, the location of the maximum undercooling can be at negative z-positions, behind the columnar tips. Note from Fig. 6 that the magnitude and location of the maximum undercooling vary with the temperature gradient in a non-monotonic fashion. As the temperature gradient is increased from Case 1, the maximum undercooling first increases (Cases 3–5) and then decreases (Cases

6 and 7) below the Case 1 value. Overall, Fig. 6 indicates that the formation of equiaxed grains in the present simulations will depend not only on the magnitude of the nucleation undercooling, but also on the thermal gradient and the position of the seeds within the columnar array.

4.2. CET

After steady columnar growth is achieved in a simulation, a regular pattern of seeds is introduced into the computational domain ahead of the columnar tips, as described in Section 3. The seeds are allowed to grow into equiaxed grains if the local constitutional undercooling in the melt at the location of a seed reaches the specified nucleation undercooling. Then, the simulations are continued until a new steady growth stage is reached. Based on the appearance of the grain structure at this new steady state, a determination can be made as to whether a CET occurs. The final grain structures obtained for each of the 29 simulations are summarized in Table 3.

Plots of the computed grain structures (i.e., contours of the phase field) are provided in Figs. 7–12 for most of the present simulation cases. These figures all follow the same format, but require some explanation. The plots are divided into two rectangular boxes. The left side of the left box shows the phase-field contours during the initial transient, until the left side of the simulation domain reaches the cut-off temperature T_c (see Section 3). The right side of the left box shows the phase-field contours at a constant temperature, corresponding to T_c. In other words, the region on the plots where T_c is equal to a constant value should not be interpreted as the structure of the mushy zone at a certain instant of time, but as the structure that is viewed by an observer who is traveling at the pulling speed and is always located at the point where the temperature is equal to T_c. The right box shows the phase-field contours in the simulation domain at the instant of time a simulation is stopped. Hence, it does represent the grain structure for a stationary observer and allows for an examination of the growth pattern during the final steady growth stage, long after the seeds are introduced. Note that the seeds are indicated in the plots as small filled circles, regardless of whether equiaxed grains originate from them or not.

Fig. 7 shows the grain structures for Cases 1–8, where the applied temperature gradient G is varied from 140 K/cm to 21,000 ($=140\times150$) K/cm. All other simulation parameters, including the pulling speed, are held constant (see Table 3). It can immediately be seen that the final grain structure is equiaxed for temperature gradients below and including 140×50 K/cm (Cases 1–5), and columnar for $G\geqslant140\times60$ K/cm (Cases 6–8). Hence, the CET occurs at a well-defined temperature gradient between 140×50 and 140×60 K/cm. Several additional observations can be made. The equiaxed growth patterns in Cases 1–5 change considerably with the applied temperature gradient. For the lowest temperature gradient (Case 1), the equiaxed

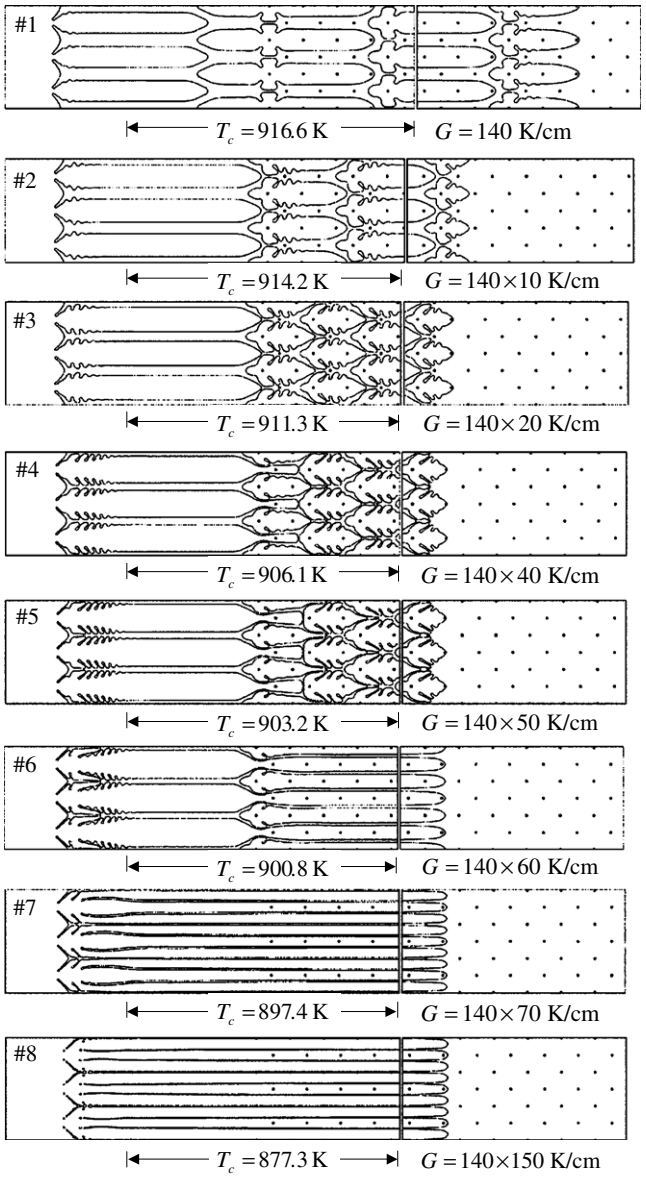

Fig. 7. Effect of the applied temperature gradient G on the CET for $V_p = 3000$ μm/s, $\Delta T_n = 8$ K, $d_s = 9.7$ μm, and $\varepsilon = 0.01$.

grains are quite elongated and feature no secondary branches. Only one out of seven seeds evolves into an equiaxed grain. The melt at the location of the inactive seeds never reaches the specified nucleation undercooling, due to solute rejection from equiaxed grains growing nearby. The rendering of seeds (i.e., grain refiner particles) as inactive by solutal interactions with growing grains, for the case of directional solidification, has also been noted by Quested and Greer [27]. For Case 5, one out three seeds nucleates, and the equiaxed grains have numerous side branches and are less elongated. Furthermore, it can be seen that the first row of equiaxed grains is almost able to continue to grow past the second row of equiaxed grains, without being blocked. Just a slight increase in the temperature gradient, to that of Case 6, allows the first row of equiaxed grains to continue to grow along with the

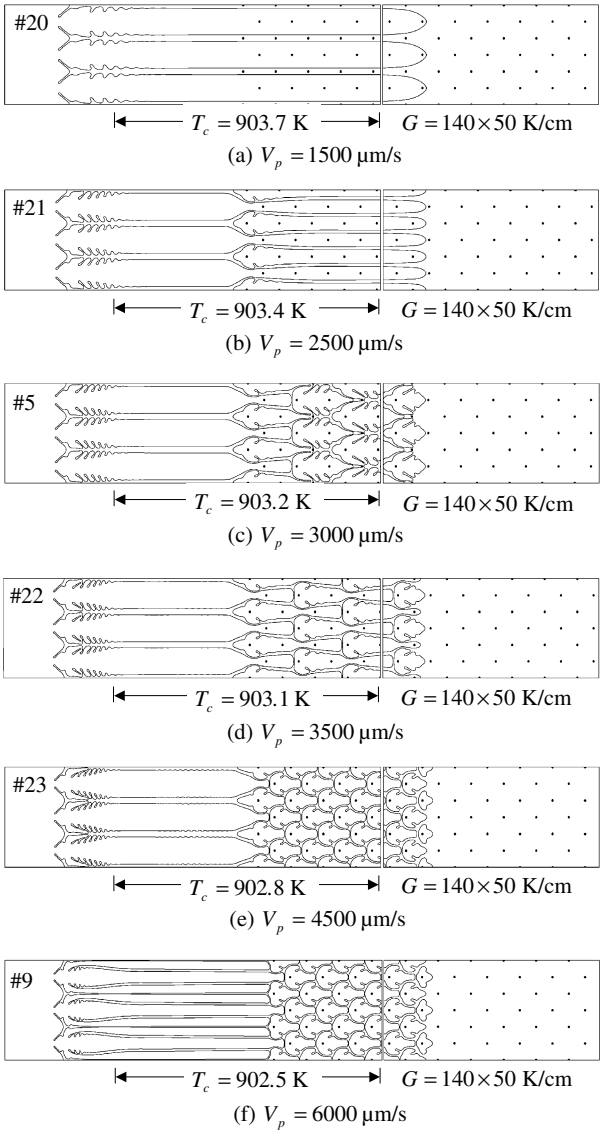

Fig. 8. Effect of the pulling speed V_p on the CET for $G = 140 \times 50$ K/cm, $\Delta T_n = 8$ K, $d_s = 9.7$ μm, and $\varepsilon = 0.01$.

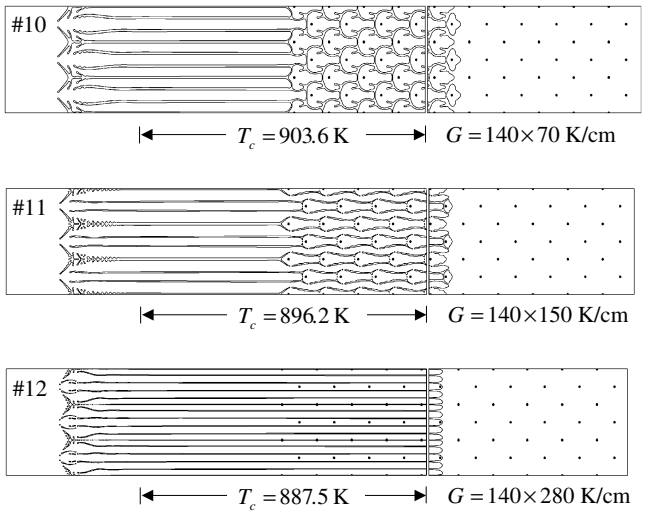

Fig. 9. Effect of the applied temperature gradient G on the CET for a high pulling speed of $V_p = 6000$ μm/s, and $\Delta T_n = 8$ K, $d_s = 9.7$ μm, and $\varepsilon = 0.01$.

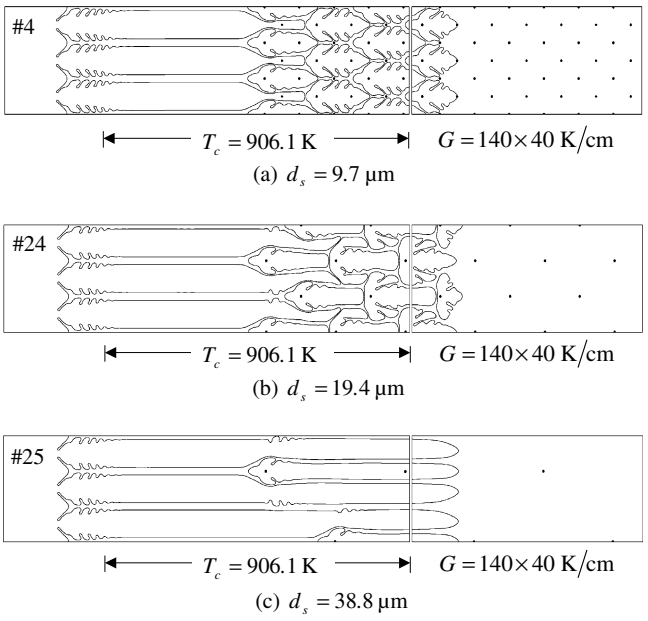

Fig. 10. Effect of the seed spacing d_s on the CET for $G = 140 \times 40$ K/cm, $V_p = 3000$ μm/s, $\Delta T_n = 8$ K, and $\varepsilon = 0.01$.

original columnar branches, resulting in a fully columnar structure at steady state. Case 6 is interesting because even though the first row of seeds nucleates, the structure remains columnar. Hence, the nucleation simply serves to adjust the columnar spacing. Both primary spacings in Case 6, before and after the introduction of the seeds, are stable; i.e., no matter how long the simulation is continued, no other equiaxed grains will nucleate and the primary spacing is constant. This indicates that, as expected, the columnar spacing affects the undercooling pattern in the melt. At the two highest temperature gradients, Cases 7 and 8, the columnar spacing is even finer than in Case 6, and none of the seeds ever nucleate. The fine spacing simply evolves from the initial interface instability.

The effect of the pulling speed V_p on the CET is explored in Fig. 8. Computed grain structures are shown for six cases (Cases 20, 21, 5, 22, 23, and 9) where the pulling speed is increased gradually from 1.5 to 6.0 mm/s, while the temperature gradient and all other parameters are held constant. It can be seen that the CET occurs between a pulling speed of 2.5 mm/s (Case 21) and 3.0 mm/s (Case 5). Considerable changes in the growth pattern with pulling speed can be observed for both the columnar and the equiaxed cases. As expected, the spacing of the columnar branches decreases with increasing pulling speed (Cases 20 and 21), with the spacing adjustment occurring through nucleation of new columnar grains right after introduction of the seeds. The equiaxed grain structures also change with pulling speed (Cases 5, 22, 23, and 9). With increasing

pulling speed, the equiaxed grains become more globular, since less time is available to grow secondary branches. Also, the number density of equiaxed grains increases with increasing pulling speed, because more of the seeds nucleate. In fact, for the two highest pulling speeds (Cases 23 and 9), all of the seeds that were introduced into the simulation evolve into equiaxed grains. This can be explained by the growth rates of the equiaxed grains increasing with increasing pulling speed. An increased dendrite growth rate causes, in turn, a higher melt undercooling and shorter solute diffusion length in the liquid surrounding the equiaxed grains. Hence, nucleation of seeds is less likely to be impeded by solutal interactions from growing grains nearby. For lower pulling speeds, on the other hand, the solute diffusion lengths are so large that many of the seeds never reach the specified nucleation undercooling [27].

Another interesting effect can be observed at relatively high pulling rates. Fig. 9 illustrates the occurrence of a CET for a pulling speed of 6.0 mm/s. Three grain structures are shown, corresponding to temperature gradients of 9.80, 21, and 39.2×10^3 K/m (Cases 10–12). The final grain structure at the lowest temperature gradient (Case 10) is equiaxed. At the highest temperature gradient (Case 12), a fine columnar structure is obtained. However, at the intermediate temperature gradient (Case 11), a "mixed" structure is found to be present at steady state. This structure is called mixed, because some of the original columnar branches continue to grow between the equiaxed grains. Even though every seed forms an equiaxed grain, the equiaxed grains do not completely block the columnar growth. The columnar branches that remain between the equiaxed grains grow in a wavy manner that conforms to the staggered arrangement of the seeds. Hence, for this pulling speed, the CET can be said to occur over a range of temperature gradients, varying by about a factor of two. In fact, for an even higher pulling speed of 10 mm/s (Cases 13–17), a mixed grain structure was obtained for temperature gradients varying by at least a factor of four. As already shown in Fig. 7 (for $V_p = 3.0$ mm/s), at lower pulling speeds the transition occurs at a sharp and well-defined temperature gradient and no mixed structures exist.

The effect of the spacing of the seeds for the nucleation of equiaxed grains on the CET is investigated in Fig. 10. The results of three simulations are shown in this figure corresponding to $d_s = 9.7$, 19.4, and 38.8 μm (Cases 4, 24, and 25, respectively), with all other parameters held constant. It can be seen that the transition from equiaxed to columnar growth occurs between Cases 24 and 25. For large seed spacings, columnar growth is favored, since the equiaxed grains are not close enough to each other to block the columnar front. Note from Case 25 that nucleation of the first row of seeds serves to adjust the columnar spacing; however, none of the subsequent seeds nucleate and the structure is indeed columnar at steady state. Comparing the results for Cases 4 and 24, it can be seen that the seed spacing has a strong effect on the equiaxed grain structure, even though the pulling speed and the temperature gradient are not changed. A larger seed spacing results in fewer equiaxed grains; thus, the grains can grow larger and also become more elongated in the direction of the applied temperature gradient. Note that a reduction in the seed spacing by a factor of two implies an increase in the number density of seeds by a factor of four (recall that $n_s = d_s^{-2}$). However, it can be seen from Fig. 10 that there are only twice as many equiaxed grains per unit area in Case 4 as in Case 24. This is because equiaxed grains nucleate only from every second seed in Case 4, while each seed nucleates in Case 24.

Fig. 11 shows a CET due to a change in the nucleation undercooling for equiaxed grains ΔT_n from 8 K (Case 6) to 7 K (Case 26). For the temperature gradient (i.e., 140×60 K/cm) and other conditions corresponding to Cases 6 and 26, Fig. 6 shows that during steady columnar growth the maximum melt undercooling is between 7 and 8 K, both in front of (Fig. 6(a)) and between (Fig. 6(b)) the columnar tips. Since the nucleation undercooling of 8 K in Case 6 is higher than the maximum constitutional undercooling of the melt, no equiaxed grains can nucleate and the structure remains columnar. For the nucleation undercooling of 7 K (Case 26), the seeds can become active and the structure becomes equiaxed.

Finally, the effect of the crystalline anisotropy strength ε on the CET is explored in Fig. 12. Results are shown for $\varepsilon = 0.5\%$, 1.0%, 1.2%, and 3%, corresponding to Cases 27, 4, 28, and 29, respectively. It can immediately be seen that for the two lower anisotropies the final grain structure is equiaxed, whereas it is columnar for the two higher anisotropies. Hence, the CET occurs sharply at an anisotropy somewhere between 1% and 1.2%. This effect has not been observed before and is not taken into account in any previous model of the CET. Variations in the anisotropy strength cause changes in the melt undercooling pattern during steady columnar growth. For example, a comparison of Cases 27 and 28 shows that an increase in the anisotropy strength from 0.5% to 1.2% results in a decrease in the steady columnar branch spacing by a factor of four. Also, with increasing anisotropy the dendrite tips become more pointed. All of these changes in the colum-

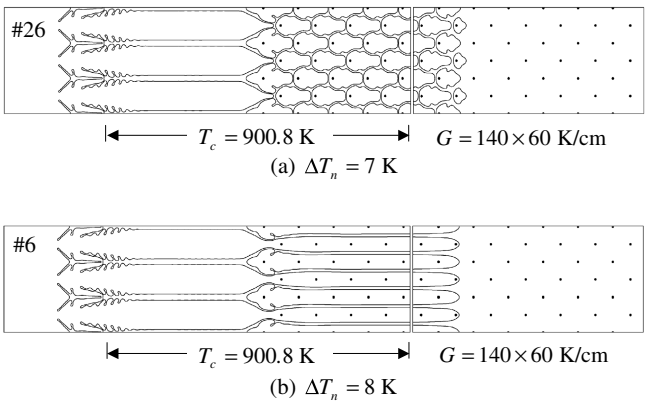

Fig. 11. Effect of the nucleation undercooling ΔT_n on the CET for $G = 140 \times 60$ K/cm, $V_p = 3000$ μm/s, $d_s = 9.7$ μm and $\varepsilon = 0.01$.

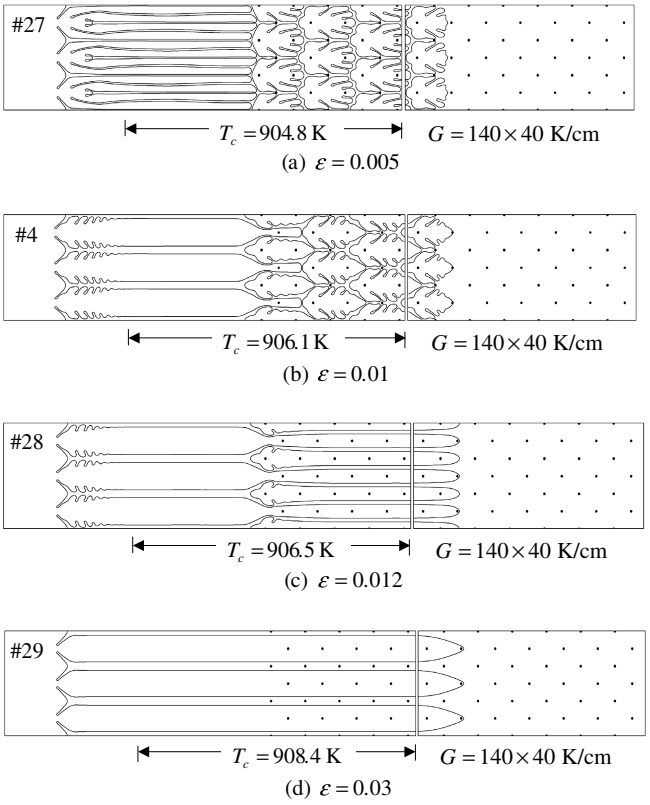

Fig. 12. Effect of the anisotropy strength ε on the CET for $G = 140 \times 40$ K/cm, $V_p = 3000$ μm/s, $\Delta T_n = 8$ K, and $d_s = 9.7$ μm.

nar growth pattern with anisotropy strength cause different melt undercooling patterns, which in turn affect the nucleation of equiaxed grains at the columnar front. While the crystalline anisotropy is a material property that cannot be independently varied in an experiment, it is nonetheless interesting to see how sensitive the CET is to this property.

4.3. Grain structure transition map

The results for the first 23 simulation cases in Table 3 are plotted on a pulling speed V_p versus temperature gradient G map in Fig. 13. These 23 cases all correspond to $\Delta T_n = 8$ K, $d_s = 9.7$ μm, and $\varepsilon = 1\%$. Equiaxed, columnar, and mixed grain structures are indicated as different symbols on the map. It can be seen that equiaxed growth generally occurs for high pulling speeds and low temperature gradients. Conversely, columnar growth is generally favored for low pulling speeds as well as for high temperature gradients. Mixed grain structures are observed at high pulling speeds and high thermal gradients.

The present results can be better understood by comparing them with Hunt's analytical model for the CET [2]. A two-dimensional version of this model can be written as

$$G = 0.666 n^{1/2} \Delta T_t \left[1 - \left(\frac{\Delta T_n}{\Delta T_t} \right)^3 \right], \tag{7}$$

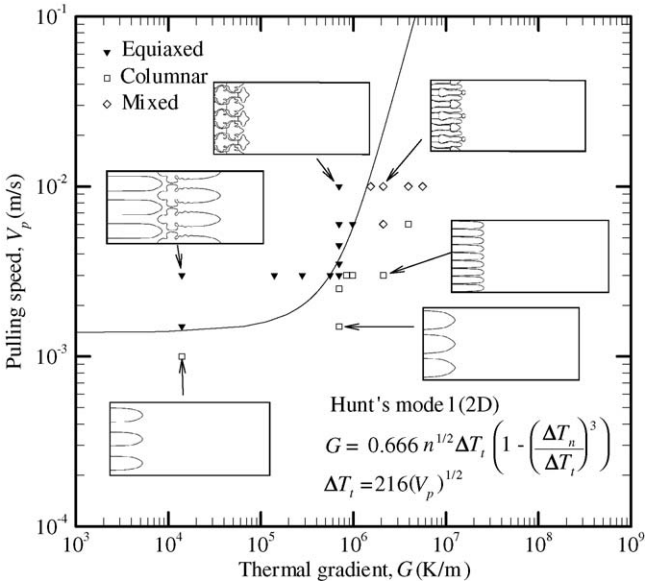

Fig. 13. CET map for directional solidification of an Al–3 wt.% Cu alloy; the symbols denote the phase-field simulation results for Cases 1–23; the solid line represents a two-dimensional version of Hunt's analytical model [2] ($\Delta T_n = 8$ K, $n = 10^{10}$ m^{-2}, and $\varepsilon = 0.01$).

where $\Delta T_t = T_l(C_\infty) - T_t$ is the undercooling of the dendrite tips measured relative to the liquidus temperature corresponding to the initial alloy composition (C_∞), and n is the number of equiaxed grains per unit area. Equiaxed (columnar) growth occurs if the temperature gradient is less than (above) the value given by Eq. (7). Eq. (7) differs from the original three-dimensional model [2] in two aspects: (1) the three-dimensional version is based on the number of equiaxed grains per unit volume and, thus, includes $n^{1/3}$ instead of $n^{1/2}$; and (2) the pre-factor, which is based on a number of geometrical considerations [2], is equal to 0.617 in the three-dimensional version, instead of 0.666. The derivation of the two-dimensional version is not presented here due to space limitations.

In the derivation of Hunt's model [2], the tip undercooling is assumed to be given as a function of the applied pulling speed by a relation of the form $\Delta T_t \propto V_p^{1/2}$, where the constant of proportionality is a function of material properties only. For the present two-dimensional simulations, such a relation can be obtained by "measuring" the temperature of the dendrite tips as a function of the imposed pulling speed during the steady columnar growth regime with which the simulations are always started. However, it was soon realized that the tip temperature: (i) also depends on the applied temperature gradient, and (ii) is not exactly proportional to $V_p^{1/2}$ even for a constant temperature gradient. This is well known from more sophisticated dendrite tip growth models [25]. Nonetheless, as a first approximation, the following fit was obtained from the results of the present simulations:

$$\Delta T_t = 216 V_p^{1/2}, \tag{8}$$

where the constant of proportionality has units of $K(s/m)^{1/2}$. Again, this relation is very approximate and becomes highly inaccurate for low temperature gradients.

The curve given by Eqs. (7) and (8) is included on the $V_p - G$ map in Fig. 13. As another rough approximation, the number density of equiaxed grains was taken equal to the seed density in the simulations, i.e., $n = n_s = d_s^{-2} = 1.06 \times 10^{10}$ m^{-2}. As was noted in the previous sub-section, not all seeds evolve into equiaxed grains when a CET occurs. Despite all of these approximations, the curve corresponding to Hunt's model can be seen to reasonably well separate the equiaxed and columnar grain structures obtained in the present phase-field simulations. Attempts (not shown here) to incorporate an improved dendrite tip growth model or to use different values for the number density of equiaxed grains in Hunt's model did not result in consistently better agreement. The comparison in Fig. 13 should only be viewed as an attempt to better understand the present predictions relative to Hunt's model. The approximate agreement indicates that the dependence of the CET on the temperature gradient and the pulling speed observed in the present simulations can be well explained by the physical considerations inherent in Hunt's model. In particular, the simulation results are in agreement with the different regimes that can be identified on the map: at low G, the CET occurs at a constant V_p; at high G, the line separating the two grain structures has a slope of unity on the log–log plot. Obviously, the mixed grain structures obtained in the simulations for high pulling speeds are not predicted by Hunt's model. These mixed grain structures can be thought of as smearing out the transition at high V_p.

5. Conclusions

Fully resolved, direct microstructure simulations of the CET in directional solidification of an Al–3 wt.% Cu alloy have been performed using a recently developed phase-field model. The results illustrate the full complexities of the solute concentration fields and solidification morphologies that are possible. The effects of the applied temperature gradient and pulling speed, the equiaxed seed spacing and nucleation undercooling, and the crystalline anisotropy strength on the CET are investigated in a parametric study. The dependence of the CET on the temperature gradient and pulling speed, found from the phase-field simulations, qualitatively agrees with the analytical CET model of Hunt [2]. More exact comparisons are not possible because the dendrite tip growth and equiaxed grain nucleation phenomena are more complex in the phase-field simulations than can easily be captured by an analytical model. Additional findings from the phase-field simulations include a mixed columnar–equiaxed structure at high pulling speeds and a strong dependence of the CET on the anisotropy strength. The present simulations also reveal a number of other interesting phenomena related to purely columnar and equiaxed growth under an applied temperature gradient. For example, solutal interactions from growing equiaxed grains can render a large fraction of seeds inactive (as already noted in Ref. [27]). The columnar branch spacing depends not only on the temperature gradient and the pulling speed, but also on the anisotropy strength; furthermore, a spacing adjustment can occur through initiation of seeds that develop into new columnar grains. Some of these phenomena deserve more detailed research attention.

There are several obvious advances that need to be made before the present microstructure simulations can be compared to experimental results. The simulations need to be extended to three dimensions and arbitrary crystallographic orientations. In addition, the effects of melt convection and the movement of seed particles and small equiaxed grains due to gravity should be accounted for. While it is possible to construct a more comprehensive phase-field model that includes these effects, numerical simulations on the scale of typical experiments will have to await the availability of more powerful computers.

Acknowledgement

This work was supported by NASA under Grant No. NNM04AA18G.

References

[1] Winegard WC, Chalmers B. Trans ASM 1954;46:1214.
[2] Hunt JD. Mater Sci Eng 1984;65:75.
[3] Flood SC, Hunt JD. J Cryst Growth 1987;82:543.
[4] Flood SC, Hunt JD. J Cryst Growth 1987;82:552.
[5] Gäumann M, Bezençon C, Canalis P, Kurz W. Acta Mater 2001;49:1051.
[6] Wang CY, Beckermann C. Metall Mater Trans A 1994;25:1081.
[7] Martorano MA, Beckermann C, Gandin C-A. Metall Mater Trans A 2003;34:1657.
[8] Rappaz M, Gandin C-A. Acta Mater 1993;41:345.
[9] Gandin C-A, Rappaz M. Acta Mater 1994;42:2233.
[10] Gandin C-A, Charbon C, Rappaz M. ISIJ Int 1995;35:651.
[11] Gandin C-A. Acta Mater 2000;48:2483.
[12] Vandyoussefi M, Greer AL. Acta Mater 2002;50:1693.
[13] Spittle JA, Brown SGR. J Mater Sci 1995;30:3989.
[14] Nastac L. Acta Mater 1999;47:4253.
[15] Dong HB, Lee PD. Acta Mater 2005;53:659.
[16] Langer JS. Phys Rev A 1986;33:435.
[17] Kessler DA, Levine H. Phys Rev B 1986;33:7867.
[18] Boettinger WJ, Warren JA, Beckermann C, Karma A. Annu Rev Mater Res 2002;32:163.
[19] Karma A. Phys Rev Lett 2001;87:115701.
[20] Ramirez JC, Beckermann C, Karma A, Diepers H-J. Phys Rev E 2004;69:051607.
[21] Echebarria B, Folch R, Karma A, Plapp M. Phys Rev E 2004;70:061604.
[22] Ramirez JC, Beckermann C. Acta Mater 2005;53:1721.
[23] Karma A, Rappel W-J. Phys Rev E 1998;57:4323.
[24] Mullins WW, Sekerka RF. J Appl Phys 1964;35:444.
[25] Kurz W, Fisher D. Fundamentals of solidification. 4th ed. TTP; 1998.
[26] Greer AL, Bunn AM, Tronche A, Evans PV, Bristow DJ. Acta Mater 2000;48:2823.
[27] Quested TE, Greer AL. Acta Mater 2005;53:4643.
[28] Shan L, Napolitano RE, Trivedi R. Acta Mater 2001;49:4271.